Damping behavior of 316L lattice structures produced by Selective Laser Melting

Francesco Rosa, Stefano Manzoni, Riccardo Casati *

Department of Mechanical Engineering, Politecnico di Milano, Via G. La Masa 1, 20156 Milano, Italy

HIGHLIGHTS

- We showed the possibility to exploit SLM for producing parts that embed lattice structures to improve their damping capacity
- In the selected deformation and frequency range, lattice structures have higher damping capability than the bulk specimens
- Higher damping is due to concentration of stress in specific lattice regions, as shown by FE simulations.

GRAPHICAL ABSTRACT
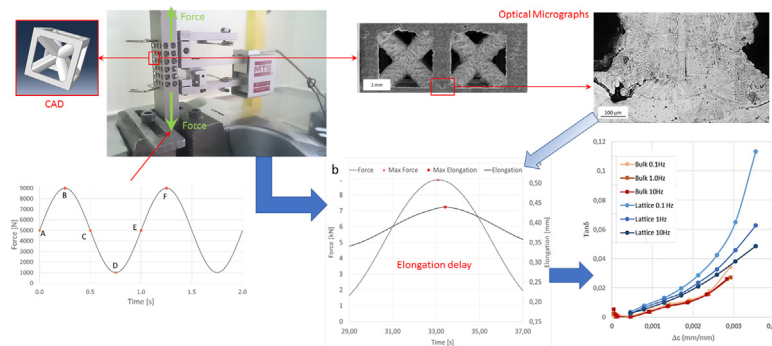
ABSTRACT

Selective Laser Melting is a powder-bed additive manufacturing technology that allows producing fully-dense metal objects with complex shapes and high mechanical properties. In this work, Selective Laser Melting was used to produce 316L specimens including lattice structures with the aim of exploring the possibility given by additive manufacturing technologies to produce parts with increased damping capacity, especially in relation to their weight. The internal friction of bulk and lattice specimens was measured in terms of delay between stress and deformation (i.e. tanδ) for different applied loads and frequencies. A finite element model was used to design the test and microstructure investigations were performed to support the results obtained by dynamo-mechanical tests.

© 2018 Elsevier Ltd. This is an open access article under the CC BY-NC-ND license (http://creativecommons.org/licenses/by-nc-nd/4.0/).

1. Introduction

Additive manufacturing (AM), also known as 3D printing, allows producing complex objects by means of a direct or layer-wise addition of material starting from 3D digital models. AM technologies were first developed for the production of prototypes, but over the years their use have been extended to the fabrication of functional and structural metal parts for service in several applications, such as turbine blades, prosthesis and medical implants, dies, valves, heat exchangers, manifolds and collectors [1–4]. Selective Laser Melting (SLM) is the most widespread 3D printing method for processing metals and it is based on the local fusion of a powder bed through a laser beam. Fully-dense parts featuring fine microstructures can be produced by SLM starting from gas-atomized powders with proper particle size distribution and morphology. The performance of SLM processed materials are comparable or even higher than those of cast and wrought products [1–4]. Several alloys are currently used for AM processes, including

* Corresponding author.
E-mail address: riccardo.casati@polimi.it (R. Casati).

AISI 316L and PH 17-4 stainless steels, Maraging steels, Inconel 625 and 718, Al-Si alloys, CoCr and Ti6Al4V [5–13]. In particular, the AISI 316L austenitic stainless steel is frequently employed due to its combination of good mechanical properties, excellent corrosion resistance and good SLM processability [5,14].

One of the most important potentialities of AM consists in the realization of geometrical shapes that cannot be manufactured otherwise. This has tremendously widened designers' possibilities but it has also led to a radical change in how parts are conceived, designed and embedded in final products.

AM technologies give the possibility to create lightweight objects by integrating three-dimensional lattice or porous structures or by topological optimization of shapes [15–17].

Periodical lattices are widely used AM solutions. They are usually obtained as a three-dimensional pattern of a unit cell specifically designed to avoid overlapping. Thus, properties of the overall lattice structures greatly depend on those of the elementary cell. Several methods are available to estimate the elastic properties of a lattice structure on the basis of elementary cell geometry and material characteristics [18]. The type and size of the unit cell and the orientation, shape, interconnections and dimension of each beam of the cell can be freely designed with the aim of customizing thermal, physical, functional and mechanical response of components. For instance, lattice structures can be used to produce optimized light and stiff structures [19], parts with peculiar mechanical characteristics, like auxetic structures with negative Poisson's ratio [20], or heat exchanger with improved thermal efficiency.

Notwithstanding several scholars are currently investigating properties of materials and parts manufactured by AM technologies and exploring new design possibilities, there are only few studies focusing on functional properties of lattice structures. So far, not many works on damping behavior of AM parts were published, even though it is a topic of extreme interest for the scientific community and for industrial applications [21,22]. In many applications, damping is indeed a desired property, especially if considered in relation to a reduction part weight: the damping capacity of lattice structures is not only important for the development of structural dampers, but it could also greatly affect the dynamic response of light structural components in which lattice are embedded.

Thus, this work is aimed at showing the possibility to exploit AM technologies for producing parts that embed lattice structures to improve their damping capacity. SLM was employed to produce 316L stainless steel specimens including lattice structure and bulk specimens. The internal friction (IF) of the two sets of samples was measured in terms of tan δ. Because of the exploratory nature of this work, it was decided to test lattice structures in the high nominal deformation region (i.e. beyond 10^{-4}), where plastic phenomena are expected to lead to higher damping, and differences between bulk and lattice structures could be more easily measurable. Finite element simulations and microstructural investigations were used as support tools for an in-depth interpretation of the experimental results.

2. Lattice geometry

A body centered cubic (BCC) cell with sides of 4 mm and beams of 1 mm in diameter has been selected for the experiments. According to Vigliotti et al. [18], in fact, this cell high structural performance since all elements fully contribute to bear the load. Thanks to this property, it was possible to design and produce lattice specimens that could be tested on the same universal testing machine used to test the bulk specimens.

The CAD model of the cell is depicted in Fig. 1a. As shown in Fig. 1b, 6 layers of 8 (4 × 2) cells were realized in a rectangular cross-section bar (8 mm × 16 mm × 150 mm).

3. Finite element model

The finite element (FE) analysis presented in this section was performed with the aim of:

1. defining topology and dimensions of specimens suitable for our universal testing machine and extensometer, and avoiding an expensive trial and error experimental procedure;
2. providing a qualitative map of the structural behavior of the lattice specimen (where the stress and strain mainly concentrate), in order to ease the description and discussion of the experimental results.

The FE analysis was carried out by ABAQUS 2017. The bars were loaded along their longitudinal axis, hence they show two symmetry planes, as shown in Fig. 1b. Thus, in order to reduce the computational efforts, only a quarter of the model was analyzed by means of the FE model. Symmetry constraints were applied on the faces generated by cutting the model. To reproduce the loading condition, the bar was fixed at one end, while the load was applied on the other end. The model has been meshed with 212,260 quadratic tetrahedral elements. A representative region of the meshed sample is shown in Fig. 2.

An elastoplastic isotropic mechanical behavior of the material has been adopted, neither ratcheting nor damping effects have been included. In this model of the material, yielding occurs if the von Mises stress exceeds the yielding strength of the material. The mechanical behavior of the material was determined using the results of tensile tests performed on standard dog-bone specimens, previously achieved by the same authors and reported in Table 1 [5]. It is worth noting that the samples used for the present experiments were realized using the same SLM system and process parameters that were adopted for producing the samples used for tensile tests. For sake of simplicity, in FE analysis, the properties of the material tested along the axis
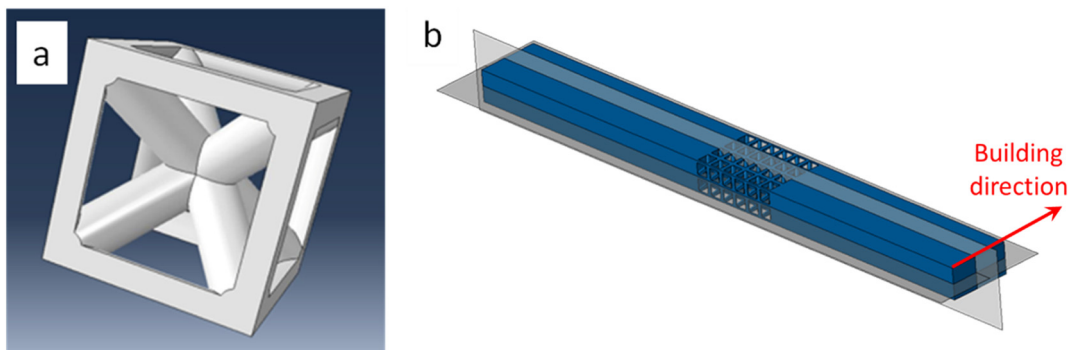

Fig. 1. a) BCC elementary cell and b) model of the specimen with symmetry planes.
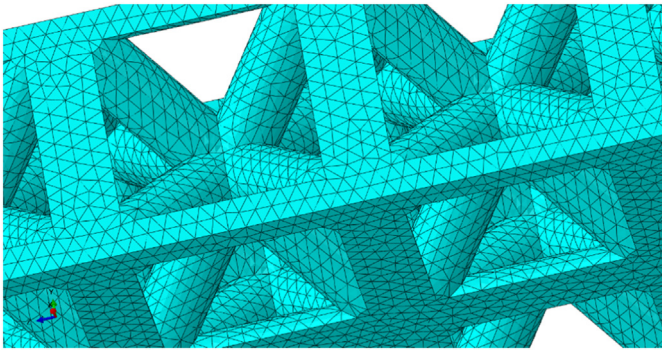
Fig. 2. Detail view of the mesh in the lattice zone.

perpendicular to the building direction were considered, since the bulk and lattice specimens were printed with the longitudinal axis parallel to building plate.

4. Materials and experimental methods

4.1. Selective Laser Melting

A Renishaw AM250 SLM system was employed for preparing specimens by using a gas-atomized AISI 316L stainless steel powder with average size of 31 μm. The chemical composition is reported in Table 2.

The specimens including lattice structures were produced according to the geometry described in Section 2. Bulk bars were also produced as reference specimens. The SLM device is equipped with a single mode fiber laser with 200 W maximum power and estimated beam diameter at focal point of 75 μm. The system utilizes pulsed wave emission, which produces discrete and partially overlapped melting spots. The hatch distance, point distance, and exposure time were set to 110 μm, 60 μm, and 80 μs, respectively. The specimens were produced under Ar atmosphere using a meander scanning strategy and a layer thickness of 50 μm.

4.2. Microstructure and surface characterization

Microstructure analysis was performed by scanning electron microscope (SEM) mod. Zeiss EVO 50 using a secondary electron detector and an operating voltage of 20 kV and by light optical microscope mod. Leitz Aristomet. Samples were prepared by standard grinding and polishing procedure and etched with $HNO_3:HCl:H_2O$ (1:1:1) solution. Surface characterization was performed by SEM after ultrasonic cleaning.

4.3. Damping tests

Damping tests were executed by means of a MTS LandMark universal testing machine equipped with 647 Side-Loading Hydraulic Wedge Grips, a system that can exert dynamic loads up to 100 kN. Tests were executed by controlling the applied force, and measuring the elongation of the lattice region by means of an extensometer (Fig. 3). The same configuration was used for bulk specimens. Tests were carried out by setting loading frequencies of 0.1, 1.0 and 10.0 Hz. According to ABAQUS analysis, 8.0 kHz and 5.3 kHz are the lowest natural frequencies of axial modes of the bulk and the lattice specimens, respectively. Therefore, any excitation near to sample resonance was avoided. The load

Table 1
Mechanical properties of 316L steel produced by SLM [5].

Direction	Yield strength (MPa)	Ultimate tensile strength (MPa)
Normal to building direction	554.0	684.7
Parallel to building direction	–	580.7

Table 2
Chemical composition of 316L powder (mass%).

	C	Si	Cr	Ni	Mn	Mo	Fe
316L	<0,03	0,5	17,0	12,0	1,5	2,5	Bal.

levels, from 1 to 9 kN for lattice samples and from 1 to 51 kN for bulk samples, were defined on the basis of the FE analysis results (which are described in the next section) in order to induce plastic deformations at the higher loads and to achieve similar elongation levels both in the lattice and bulk specimens.

The value of tan δ, at each tested amplitude and frequency values, was evaluated by estimating the phase difference between the acquired sinusoidal time-signals of force and elongation in steady-state (i.e. with the shift of the mean value of the elongation signal at regime). Different algorithms were used to estimate the phase values, without noticing any significant difference in terms of results. The final approach used was the least squares fit of the sinusoidal time-signals [23], often called three–parameter least squares fit. This method allows to calculate the time-delay between the two signals, which is then used to compute the phase difference.

5. Results of the FE analyses

FE analyses were carried out to define the maximum load that samples can bear by avoiding failures, and to determine the regions of the specimens in which plastic deformation mainly occurs for a better interpretation of mechanical tests.

Fig. 4 depicts the maximum principal stress and the logarithmic strain distributions within the lattice region at several stages of the loading cycle when the maximum load amplitude is applied on a new specimen (i.e. not subjected to previous cycling loads). The maximum value of the scale has been fixed at 554 MPa, i.e. the yield strength of the material.

It is worth observing that yielding first occurs in the beams parallel to the loading direction and at beams junctions. When the load first reaches the mean value (5 kN, at point A), the beams parallel to the loading direction are fully yielded and correspond to the highest deformed regions within the lattice. Diagonal beams exhibit a much lower logarithmic deformation, whereas their displacement is guaranteed by the yielding of the junctions at the center of the elementary cells. This mechanism becomes even more evident when the load reaches the maximum value (9 kN, at point B). Contrary to the condition described for the point A, upon unloading to 5 kN (point C), the zones with a maximum principal stress higher than 554 MPa are noticeable at the central junctions, whereas the longitudinal beams appear highly

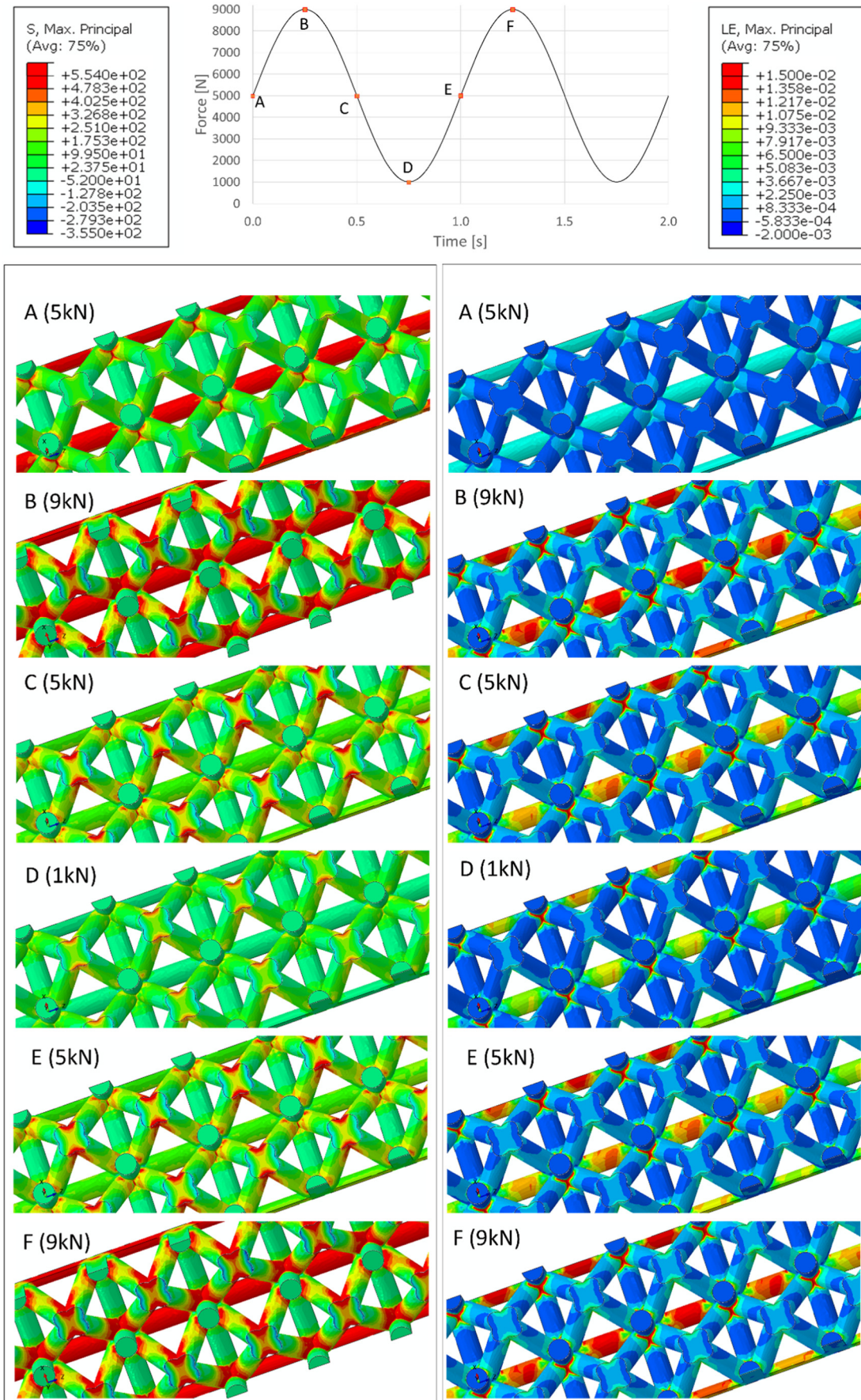**Fig. 3.** Experimental setup for dynamic tests.

Fig. 4. Maximum principal stress and maximum principal logarithmic strain distributions in the quarter model as a function of the applied axial load.
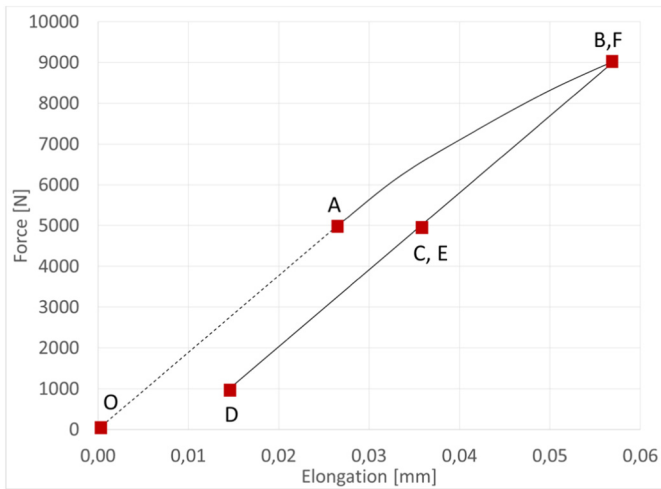
Fig. 5. FEM force-elongation relationship.

deformed. An analogous stress/strain configuration, but to a lower extent, occurs at 1 kN (point D). When the load reaches the mean and maximum values for the second time (point E and point F), the sample exhibits the same stress and strain distributions of the condition corresponding to the points C and B, respectively. As the test continues, the specimen repeatedly undergoes to the stress and strain distributions of points C, D, E and F. From an overall point of view (Fig. 5), during the first loading up to the maximum load (O ➔ B), it is possible to observe an initial linear elastic behavior of the structure, then the effect of the yielding. After point B, the behavior of the lattice is fully elastic and no accumulation of plastic deformation is predicted by the FE model. As mentioned in the Section 3, indeed, this model does not take into account ratcheting phenomenon; accordingly, the structure dissipate energy only during the first loading (up to point B), when the material is yielded for the first time.

Because of yielding of some lattice regions, residual stresses and strains develop upon unloading. Fig. 6a shows the residual stress due

to the application of a 9 kN axial load. The darker areas at the junction between vertical and horizontal beams exhibit residual compressive state of stress, whereas the diagonal beams reveal to be under tensile stress in the elastic range.

Fig. 6b shows the corresponding residual strains. They consist in an elongation of the longitudinal beams and a concentration of the deformation at the beam junction due to a variation of the angle between the diagonal beams.

In the light of these analyses, it was concluded that 9 kN can be borne by the considered lattice structure with no risk of failures and are able to induce high elasto-plastic deformations within the lattice that in turn should be responsible for high damping levels.

6. Experimental results

6.1. Morphological and microstructural characterization of the specimens

Solid and lattice specimens were produced by SLM, two representative samples are shown in the picture of Fig. 7a. The external surfaces of the lattice structures were analyzed by SEM, representative micrographs are reported in Fig. 7b, c and d. The surface appears rough and several defects were detected. On the underside of overhangs, partially molten powder particles and partially molten sputters were noticeable, as that indicated by the arrow in the micrograph of Fig. 7c. On top surfaces a few spattered particles were also found, as shown in Fig. 7d.

The as-build samples exhibited solidification tracks on the macroscale and evidence of a solidification structure on the micro-scale (Fig. 8). In Fig. 8a, a characteristic optical micrograph of the lateral section of a lattice sample is shown. Periodic melt pools generated by the scanning of the laser over the powder-bed are made evident by chemical etching. At higher magnification (Fig. 8b), a fine cellular substructure is revealed. Elongated cells with different spatial orientation are about 1 μm in diameter and a few microns in length and grew across melt pool boundaries, suggesting epitaxial growth from re-melted zones. It is worth noting that some internal defects, mainly pores, were found in the specimens. At a few beam junctions cracks that developed along the melt pool boundaries were visible (Fig. 8a).
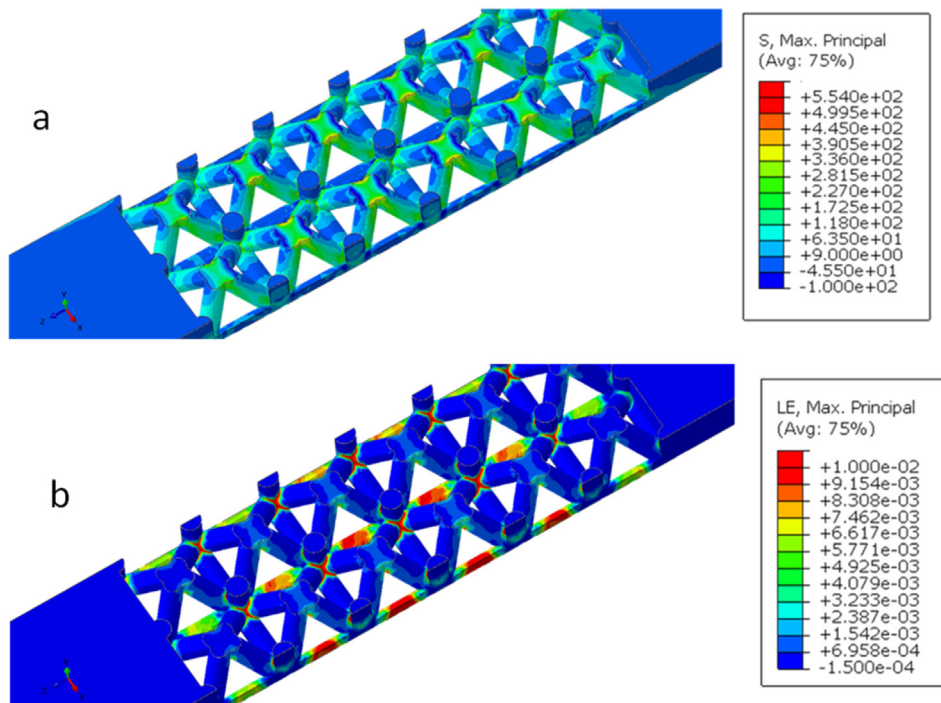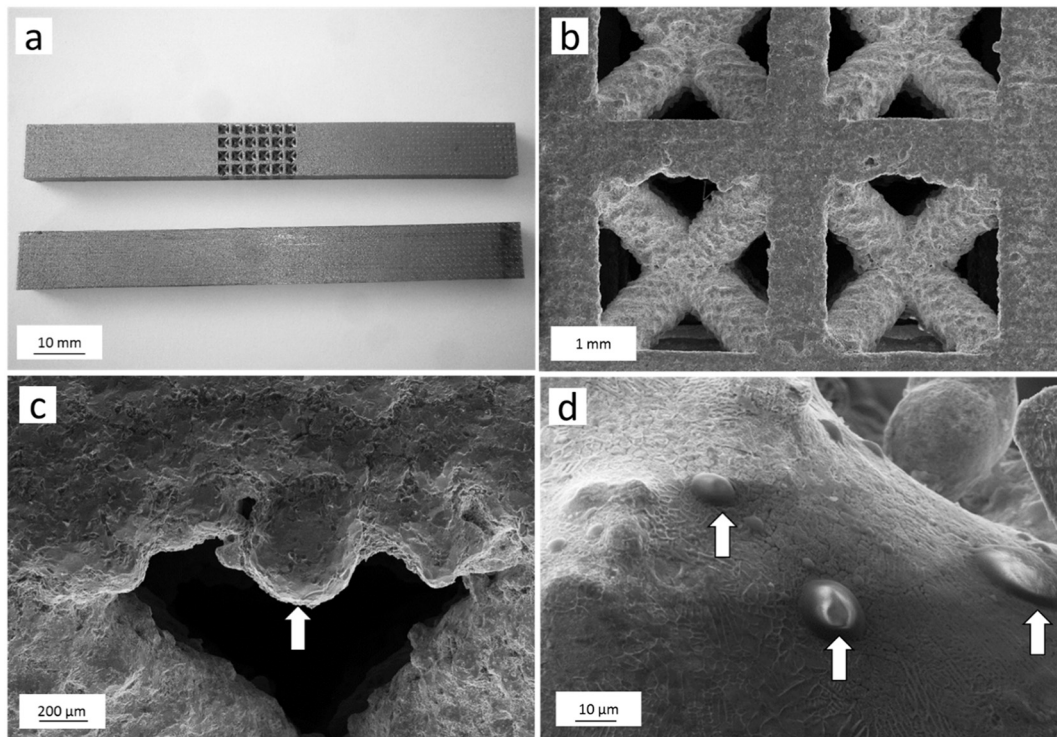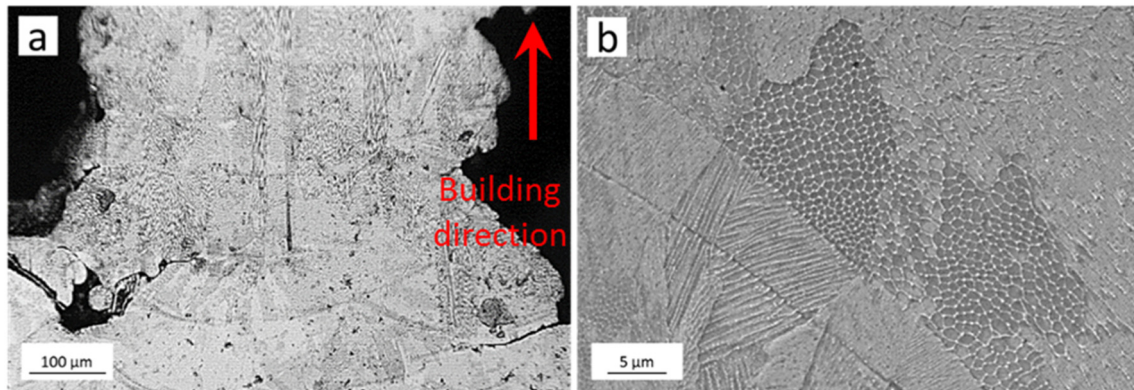

Fig. 6. Max principal residual stress and logarithmic (true) residual strain after having applied a 9 kN axial load.

Fig. 7. a) Picture of two representative specimens; SEM images (building direction is upwards) of b) a lattice structure, c) a particle sintered on the lower face of a beam and d) sputtered particles on the upper face of a beam.

Fig. 8. Micrographs of a lattice specimen at a) low and b) high magnification.

For comparison, in Fig. 9, the microstructure of a bulk sample is reported. Contrary to the lattice, bulk samples do not show large defects. The solidification cell size of bulk and lattice specimens was similar.

6.2. Damping tests results

Damping tests were performed at 0.1, 1 and 10 Hz. Ratcheting occurs during the first loading cycles, as depicted in Fig. 10a for the test performed between 1 and 9 kN at 0.1 Hz. No substantial variation in strain amplitude was detected, if initial and stabilized cycles are compared.

In Fig. 10b, a close-up view of the curve is depicted. It is evident the gap between the time of the peaks of the stress and strain curves.

When the stress is plotted as a function of the strain (Fig. 11), the hysteresis loop shows that energy is dissipated during the loading cycles (the area enclosed between the loading and the unloading curves).

The diagrams of Fig. 12 show the computed damping capacity (tan δ) and the specific damping capacity (tanδ·m^{-1}, where m is the theoretical mass) as a function of stress ($\Delta\sigma$) and strain ($\Delta\varepsilon$) amplitudes of the cycles. The damping capacity and the specific damping capacity

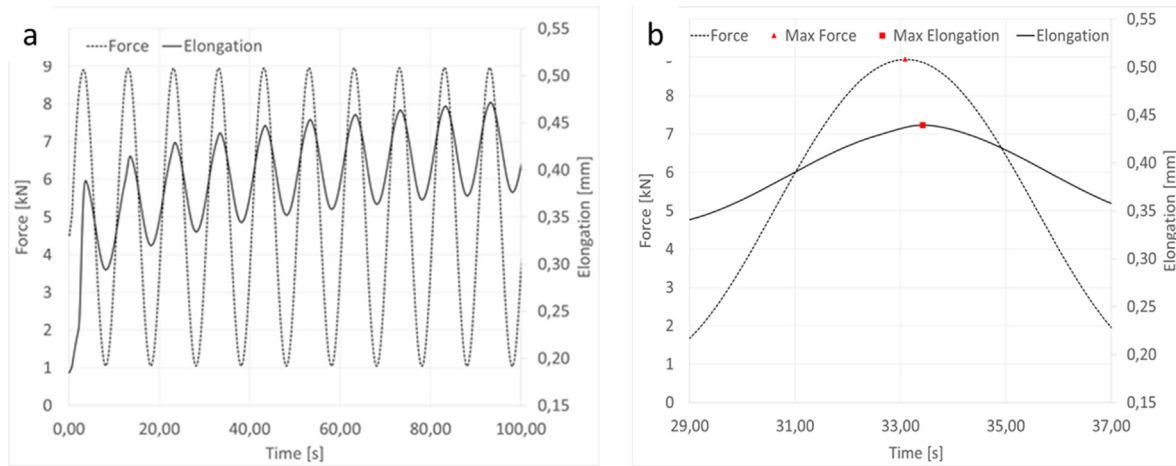**Fig. 9.** Optical micrograph of a bulk specimen.

Fig. 10. Load and elongation measured during the first 10 cycles of the 1–9 kN test at 0.1 Hz.

increase as the loading frequency is increased. Higher the applied stress (or strain), greater is the damping capacity of the material. At the same applied stress, the bulk material dissipates less energy than the lattice. Likewise, when the same strain is considered, the lattice shows higher tan δ than the bulk specimen, but to a lower extent. The damping capacity of the lattice specimen appears much more evident when it is expressed as specific tanδ.

7. Discussion

Damping capacity increases with load frequencies, which is common for many structures/systems [24,25]. The lattice show higher damping capacity than the bulk specimens either if the same $\Delta\sigma$ and $\Delta\varepsilon$ are applied for the three load frequencies considered in this work, i.e. 0.1, 1 and 10 Hz. This is much more evident when the specific damping capacity is considered. This can be attributed to the fact that the stress field is not homogeneous within the lattice and low nominal stresses are able to induce high deformations in some specific regions of the sample.

The overall damping capacity of a material is the results of several overlapping contributions and, depending on the strain amplitude range, some damping phenomena are dominant over the others.

Below a critical amplitude value (ε_{cr1}), the so-called *amplitude-independent internal friction* due to thermo-elastic currents is believed to be the main damping mechanism. Beyond ε_{cr1} *amplitude dependent*

internal friction (*ADIF*) mechanisms are active and are much more effective than the amplitude-independent ones [26]. Above a second threshold strain, ε_{cr2}, internal friction is due to micro-plastic deformations, whereas for strain amplitudes among the two critical values ($\varepsilon_{cr2} > \varepsilon > \varepsilon_{cr1}$), internal friction is the result of string-like motion of dislocations and magnetic domains walls.

A few works have been published on damping behavior of metal foams, which contain empty spaces and stress raiser sites, similarly to lattice structures [26–30]. They showed that even for very low strain amplitudes ($<10^{-5}$), damping in metal foams is not absolutely amplitude independent, but it is overlapped with ADIF mechanisms and that for strain amplitudes higher than ~10^{-4}, damping is mainly related to micro-plasticity phenomena in many materials, including 316L stainless steel produced by powder metallurgy methods [26–30]. In the load range tested in this work, even the lowest applied load (2 kN) was able to induce nominal deformation higher than $5.2 * 10^{-3}$. Since the ratio between relative modulus and relative density of the lattice investigated in this work is comparable to that of 316L foams reported in ref. [24], it can be assumed that damping mechanisms typical of metal foams can also be used for interpreting the IF phenomena occurring in the investigated lattice structures. The deformations shown by the lattices are one order of magnitude above the threshold for inducing micro-plastic phenomena in open-cell foams. Thus, it is expected that the high internal friction shown by the lattice tested in this work is mainly due to ADIF mechanisms and in particular to dislocation glide and multiplication. The presence of cracks and surface defects in lattice specimens, as shown in Fig. 8a, may also play as an additional IF contribution to the overall damping capacity of the structure. In the lattice structure, indeed, a few cracks were visible at beam junctions and several defects were detected on beam surfaces, such as partially molten particles and spatters. Therefore, defects might also be responsible for an extra frictional contribution caused by relative movement of free surfaces and strass raiser effect. The main drawback is that micro-plastic phenomena and crack propagation can lead to fatigue failure of the components, limiting the use of lattice structures to low-cycle applications when high strain amplitudes are applied. Further analyses are needed to estimate the lattice behavior at low strain amplitudes and the contribution to structural damping given by small defects at different strain amplitudes and frequencies. One should also consider that continuous process and material optimization will lead to parts containing less and less defects.

Even though metallic foams exhibit high damping capacity, similarly to what achieved by lattice in this work, there are two main advantages of AM structures over conventional cellular materials. First of all, AM gives the unique chance to directly integrate damping elements in components, adding therefore a functionality to parts with different
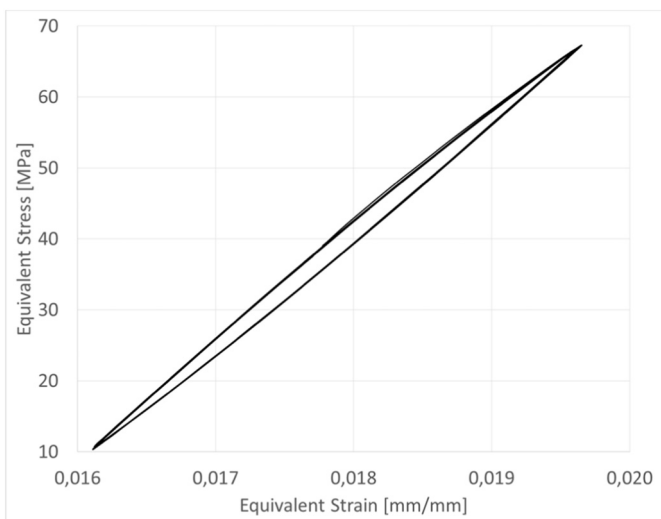

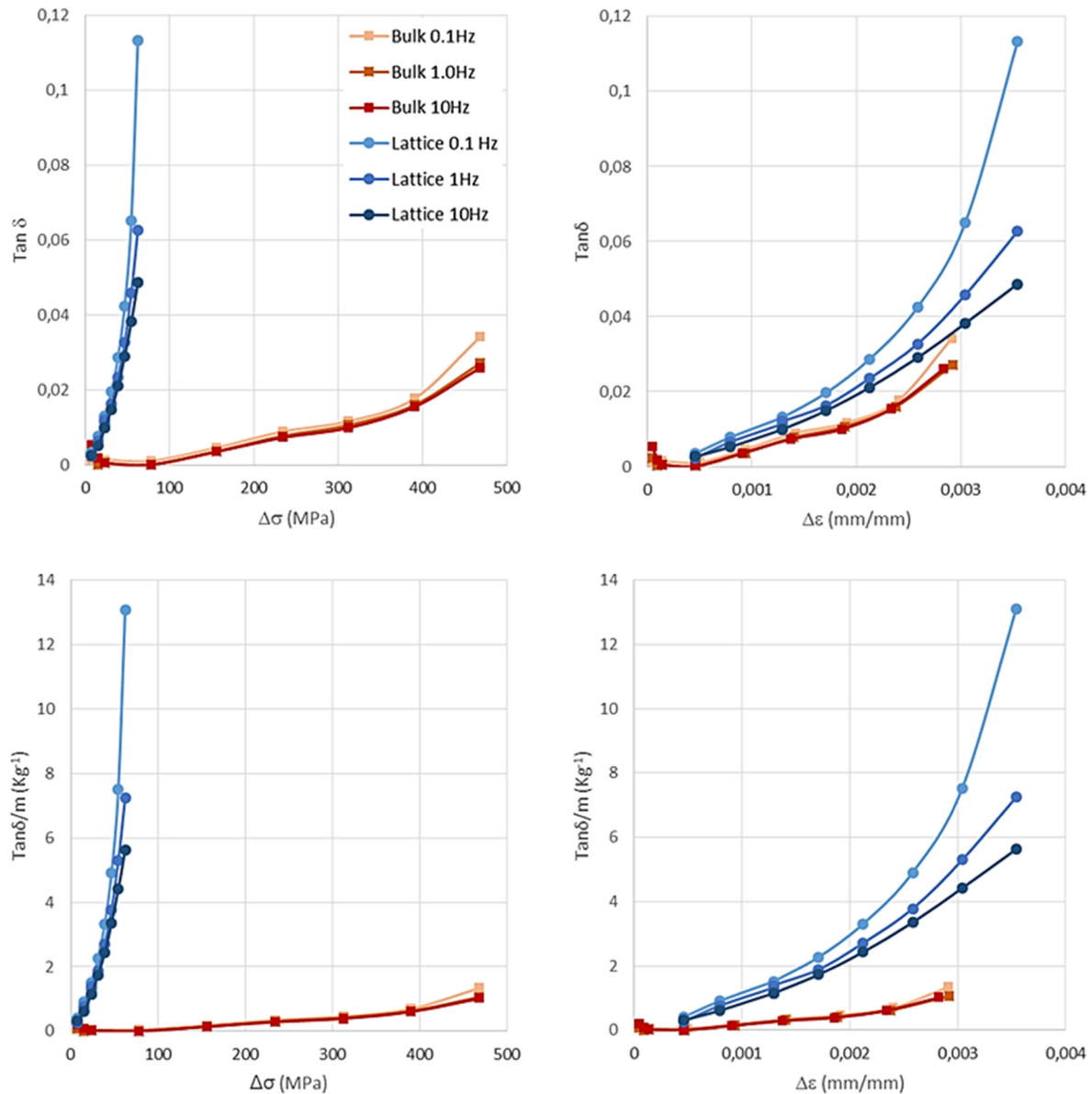Fig. 11. Equivalent stress/strain cycles at 10 Hz between 1 and 9 kN.

Fig. 12. Damping capacity (tanδ) and specific damping capacity (tanδ·m^{-1}) as a function of applied stress and strain.

structural or functional scopes. In addition, cell geometries and beam sizes can be simply customized to reach a target damping capacity of a structure.

8. Conclusion

This work showed the possibility to exploit additive manufacturing technologies for producing parts that embed lattice structures to improve their damping capacity. The internal friction of bulk and lattice samples was measured in terms of tan δ. In the selected deformation amplitude and frequency range, lattice structures have higher damping capability than the bulk specimens. This behavior is believed to be due to amplitude dependent internal friction phenomena, mainly occurring at beam joints and in the longitudinal beams. The great advantage of lattice structures produced by additive manufacturing over metallic foams is that lattice geometry can be simply customized. In addition lattices can be integrated into all parts produced by additive manufacturing technologies. On the basis of these promising results, authors will further explore damping capability of lattice structures, investigating the small deformation (below 10^{-4}) and high frequency ranges.

CRediT authorship contribution statement

R. Casati: Conceived and designed the experiments, Performed the mechanical tests, Performed the metallurgical analysis, Analyzed the data, Wrote the paper. **F. Rosa:** Conceived and designed the experiments, Performed the mechanical tests, Performed the FE analysis, Analyzed the data, Wrote the paper. **S. Manzoni:** Developed the algorithm to determine tanδ, Analyzed the data, Wrote the paper.

References

[1] T. DebRoy, H.L. Wei, J.S. Zuback, T. Mukherjee, J.W. Elmerb, J.O. Milewskic, A.M. Beesea, A. Wilson-Heida, A. De, W. Zhang, Additive manufacturing of metallic components – process, structure and properties, Prog. Mater. Sci. 92 (2018) 112.

[2] H. Fayazfar, M. Salarian, A. Rogalsky, D. Sarker, P. Russo, V. Paserin, E. Toyserkani, A critical review of powder-based additive manufacturing of ferrous alloys: process parameters, microstructure and mechanical properties, Mater. Des. 144 (2018) 98–128.

[3] Y. Kok, X.P. Tan, P. Wang, M.L.S. Nai, N.H. Loh, E. Liu, S.B. Tor, Anisotropy and heterogeneity of microstructure and mechanical properties in metal additive manufacturing: a critical review, Mater. Des. 139 (2018) 565–586.

[4] M.G. Rashed, M. Ashraf, R.A.W. Mines, P.J. Hazell, Metallic microlattice materials: a current state of the art on manufacturing, mechanical properties and applications, Mater. Des. 95 (2016) 518–533.

[5] R. Casati, J. Lemke, M. Vedani, Microstructure and fracture behavior of 316L austenitic stainless steel produced by selective laser melting, J. Mater. Sci. Technol. 32 (2016) 738–744.

[6] C.G. Kasperovich, J. Haubrich, J. Gussone, G. Requena, Correlation between porosity and processing parameters in TiAl6V4 produced by selective laser melting, Mater. Des. 105 (2016) 160–170.

[7] R. Casati, M. Vedani, Aging response of an A357 Al alloy processed by selective laser melting, Advanced Engineering Materials, 2018, (In press).

[8] J. Fiocchi, A. Tuissi, P. Bassani, C.A. Biffi, Low temperature annealing dedicated to AlSi10Mg selective laser melting products, J. Alloys Compd. 695 (2017) 3402–3409.

[9] R. Casati, J.N. Lemke, A. Tuissi, M. Vedani, Aging behaviour and mechanical performance of 18-Ni 300 steel processed by selective laser melting, Metals 6 (2016) 218–228.

[10] P. Wang, B. Zhang, C. Cheh Tan, S. Raghavan, Y.-F. Lim, C.-N. Sun, J. Wei, D. Chi, Microstructural characteristics and mechanical properties of carbon nanotube reinforced Inconel 625 parts fabricated by selective laser melting, Mater. Des. 112 (2016) 290–299.

[11] T.D. McLouth, G.E. Bean, D.B. Witkin, S.D. Sitzman, P.M. Adams, D.N. Patel, W. Park, J.-M. Yang, R.J. Zaldivar, The effect of laser focus shift on microstructural variation of Inconel 718 produced by selective laser melting, Mater. Des. 149 (2018) 205–213.

[12] F.S. Schwindling, M. Seubert, S. Rues, U. Koke, M. Schmitter, T. Stober, Two-body wear of CoCr fabricated by selective laser melting compared with different dental alloys, Tribol. Lett. 60 (2015) 25.

[13] L.E. Murr, E. Martinez, J. Hernandez, S. Collins, K.N. Amato, S.M. Gaytan, P.W. Shindo, Microstructures and properties of 17-4 PH stainless steel fabricated by selective laser melting, J. Mater. Res. Technol. 1 (2012) 167–177.

[14] L. Liu, Q. Ding, Y. Zhong, J. Zou, J. Wu, Y.-L Chiu, J. Li, Z. Zhang, Q. Yu, Z. Shen, Dislocation network in additive manufactured steel breaks strength–ductility trade-off, Mater. Today 21 (2018) 354–361.

[15] S.L. Sing, F.E. Wiria, W.Y. Yeong, Selective laser melting of lattice structures: a statistical approach to manufacturability and mechanical behaviour, Robot. Comput. Integr. Manuf. 49 (2018) 170–180.

[16] D. Wang, Y. Yang, R. Liu, D. Xiao, J. Sun, Study on the designing rules and processability of porous structure based on selective laser melting (SLM), J. Mater. Process. Technol. 213 (2013) 1734–1742.

[17] Y. Xu, D. Zhang, Y. Zhou, W. Wang, X. Cao, Study on topology optimization design, manufacturability, and performance evaluation of Ti-6Al-4V porous structures fabricated by selective laser melting (SLM), Materials 10 (2017) 1048.

[18] A. Vigliotti, D. Pasini, Stiffness and strength of tridimensional periodic lattices, Comput. Methods Appl. Mech. Eng. 229–232 (2012) 27–43.

[19] X. Zheng, H. Lee, T.H. Weisgraber, M. Shusteff, J. DeOtte, E.B. Duoss, C.M. Spadaccini, Ultralight, Ultrastiff mechanical metamaterials, Science 344 (6190) (2014) 1373–1377.

[20] T. Buckmann, R. Schittny, M. Thiel, M. Kadic, G.W. Milton, M. Wegener, On three-dimensional dilational elastic metamaterials, New J. Phys. 16 (2014) 33032.

[21] R. Ramadani, A. Belsak, M. Kegl, J. Predan, S. Pehan, Topology optimization based design of lightweight and low vibration gear bodies, Int. J. Simul. Modell. 17 (1) (2018) 92–104.

[22] Damping of selective-laser-melted NiTi for medical implants, J. Mater. Eng. Perform. 23 (7) (July 2014) 2614–2619.

[23] A. Brandt, M. Berardengo, S. Manzoni, A. Cigada, Scaling of mode shapes from operational modal analysis using harmonic forces, J. Sound Vib. 407 (2017) 128–143.

[24] D.J. Ewins, Modal Testing: Theory, Practice and Application, 2nd edition Research studies press Ltd., Baldock (K), 2000.

[25] M. Colakoglu, Factors affecting damping in aluminum, J. Theor. Appl. Mech. 42 (2004) 95–105.

[26] I.S. Golovin, H.R. Sinning, Internal friction in metallic foams and some related cellular structures, Mater. Sci. Eng. A 370 (2004) 504–511.

[27] I.S. Golovin, H.R. Sinning, Damping in some cellular materials, J. Alloys Compd. 355 (2003) 2–9.

[28] I.S. Golovin, H.R. Sinning, I.K. Arhipov, S.A. Golovin, M. Bram, Damping in some cellular materials due to microplasticity, Mater. Sci. Eng. A 370 (2004) 531–536.

[29] J. Banhart, J. Baumeister, M. Weber, Damping properties of aluminium foams, Mater. Sci. Eng. A 205 (1996) 221–228.

[30] I.S. Golovin, H.R. Sinning, J. Gokhen, W. Riehemann, Fatigue-related damping in some cellular metallic materials, Mater. Sci. Eng. A 370 (2004) 537–541.